Journal of Materials Chemistry A

ROYAL SOCIETY OF CHEMISTRY

PAPER

View Article Online
View Journal | View Issue

Open Access Article. Published on 04 May 2022. Downloaded on 12/12/2024 5:26:19 PM.
This article is licensed under a Creative Commons Attribution 3.0 Unported Licence.

Check for updates

Cite this: J. Mater. Chem. A, 2022, 10, 11172

Halogenation of $Li_7La_3Zr_2O_{12}$ solid electrolytes: a combined solid-state NMR, computational and electrochemical study†

Bo Dong, *[a] Abby R. Haworth, [b] Stephen R. Yeandel, [cd] Mark P. Stockham, [a] Matthew S. James,[a] Jingwei Xiu,[a] Dawei Wang, [de] Pooja Goddard, [c] Karen E. Johnston [b] and Peter R. Slater *[a]

Received 25th August 2021
Accepted 21st February 2022

DOI: 10.1039/d1ta07309e

rsc.li/materials-a

Garnet-based solid electrolytes have been proposed as promising candidates for next generation all-solid-state batteries. Whilst multiple cation substitution studies of these garnets have been undertaken to try and improve their overall performance, anion doping of garnets has rarely been attempted, owing to the synthetic challenges associated with this particular doping strategy. In this work, we present the halogenation (F, Cl) of the solid state electrolyte $Li_7La_3Zr_2O_{12}$ (LLZO) *via* a low temperature solid state synthetic route using PTFE and PVC polymers. A reduction in tetragonal distortion (F incorporation) and a tetragonal to cubic phase transition (Cl incorporation) is observed in halogenated LLZO, suggesting the replacement of O^{2-} with F^- or Cl^- is associated with the creation of lithium vacancies. Combined solid-state NMR and computational studies support the presence of F^- or Cl^- in halogenated LLZO. The effects of surface fluorination were also investigated for Al-doped LLZO ($Li_{6.4}Al_{0.2}La_3Zr_2O_{12}$, LLAZO) with the results suggesting that this strategy has the ability to prevent full dendrite penetration at high current densities (up to 10 mA cm^{-2}).

Introduction

State-of-the-art lithium-ion batteries (LIBs) have dominated the portable electronics industry for almost three decades, owing to their outstanding cycling stability and high energy densities.[1] In recent years, the development of electric vehicles (EVs) and large-scale off-grid harvesting facilities have called for energy storage systems with higher energy densities and improved safety.[2] However, the flammable electrolytes used in conventional LIBs, typically $LiPF_6$ in an organic solvent, raises significant safety concerns in the event of thermal runaway of the cell. Consequently, current technology relies heavily upon the efficient heat management of battery packs, especially in EVs. All-solid-state batteries (ASSBs), which replace the organic liquid electrolyte with a non-flammable inorganic solid electrolyte, overcome these safety issues, whilst also being chemically stable with Li metal anodes and high voltage cathode materials. Consequently, ASSBs are being considered as potential candidates to improve both the performance and safety of LIBs.[3,4]

Amongst the plethora of ceramic electrolytes investigated, lithium-rich garnets combine relatively good electrochemical stability to Li metal with chemical stability in air and high room temperature ionic conductivities. Hence, these materials are promising potential solid electrolytes for practical applications.[5–10] The ideal garnet framework has the general formula $A_3B_2C_3O_{12}$, where A, B and C are eight, six and four oxygen coordinated sites, respectively, with space group $Ia\bar{3}d$. Stoichiometric lithium-containing garnets such as $Y_3Te_2Li_3O_{12}$ typically exhibit poor ionic conductivity, as lithium fully occupies the tetrahedral C-site, meaning there are no sites available to accommodate any mobile Li. However, in 2003, fast Li^+ ion conduction was reported by Thangadurai *et al.*[11] in the lithium-rich garnet $Li_5La_3M_2O_{12}$ (M = Nb, Ta). In these systems, in addition to Li being in the tetrahedral 24d sites, it also partially occupies the distorted octahedral 96h and 48g sites. Since this initial work by Thangadurai *et al.*, higher Li contents, of up to a maximum of 7 per formula unit have been reported, *e.g.*, $Li_7La_3Zr_2O_{12}$ (LLZO). Such an increase in Li content typically results in an increase in ionic conductivity. However, at the maximal (7) Li content, the conductivity decreases due to lithium ordering (to reduce short Li–Li distances), which reduces the symmetry from a cubic to tetragonal cell ($I4_1/acd$). This results in a structure where all of the lithium sites (tetrahedral 8a and octahedral 16f and 32g) are fully occupied.[12,13]

[a]School of Chemistry, University of Birmingham, B15 2TT, UK. E-mail: b.dong@bham.ac.uk; p.r.slater@bham.ac.uk

[b]Department of Chemistry, Durham University, DH1 3LE, UK

[c]Department of Chemistry, Loughborough University, Loughborough, LE11 3TU, UK

[d]Department of Materials Science and Engineering, The University of Sheffield, S1 3JD, UK

[e]Shenzhen Institute of Advanced Electronic Materials, Shenzhen Institute of Advanced Academy of Sciences, Shenzhen, 518055, China

† Electronic supplementary information (ESI) available. See DOI: 10.1039/d1ta07309e

This journal is © The Royal Society of Chemistry 2022

Open Access Article. Published on 04 May 2022. Downloaded on 12/12/2024 5:26:19 PM. This article is licensed under a Creative Commons Attribution 3.0 Unported Licence.

Tetragonal Li_7-based systems have a temperature dependant tetragonal to cubic phase transition, *e.g.*, $Li_7La_3Zr_2O_{12}$ transforms to a cubic phase at 725 °C.[14] This cubic phase, which is highly conductive, can be stabilised at lower temperature by the introduction of lithium vacancies *via* numerous doping strategies, including Nb, Ta on the Zr site or Al, Ga on the Li site.[15–21] The tetragonal to cubic transition in these garnets can also be facilitated by the well-known, yet highly undesirable, proton/lithium exchange that occurs in a humid atmosphere.[22–27] Structural studies have demonstrated that both the lithium content and lithium distribution within the garnet framework impact both the ion migration pathway and the ionic conductivity, with the optimum conductivity typically observed for lithium contents of 6.4–6.6 per garnet formula.[5,7,9,28,29] In addition to optimising the Li-ion conductivity of lithium-rich garnets *via* cationic doping, considerable attention has been focused on overcoming the high interfacial resistance between the electrolyte and electrodes, as well as trying to eliminate dendrite infiltration through the electrolyte.[30–38] It has been reported that the application of coatings to the garnet pellets (and consequently lithium alloying with the coating at the interface) and hybrid polymer-garnet electrolyte composite systems can mitigate these problems to a degree.[39–49] Short circuiting behaviour in the garnet system was also recently reported to be reversible, which can be healed by a low current density electrochemical process.[50,51]

Whilst there have been numerous cation doping studies of garnet-based materials, the investigation of anion doping strategies is limited, despite prior computational studies suggesting that F-doping in $La_3Zr_2Li_7O_{12}$ may be beneficial.[52–54] This omission is likely linked to the challenges associated with the preparation of such F-containing mixed metal oxides, owing to the high thermodynamic stability of the fluoride starting materials, *e.g.*, LaOF, which is a thermodynamically favoured F-containing product at the usual synthesis temperatures.[55] Additionally, F may be lost at elevated temperatures through the reaction with moisture, thereby liberating HF. To overcome this, low temperatures (typically <400 °C) and precursors with a similar structure are commonly used. To successfully achieve fluorination, a wide range of reagents have been employed, including F_2, NH_4F, and XeF_2, with the use of F-containing polymers attracting the greatest interest.[56–58] Polymers such as polyvinylidene fluoride (PVDF) and polytetrafluoroethylene (PTFE) have been widely used for the low temperature fluorination of perovskite and related mixed metal oxide systems, leading to a wide range of new oxide fluorides exhibiting interesting magnetic properties, as well as materials of interest for use in F-ion batteries.[59]

Here, we have applied polymer fluorination methods to solid electrolyte materials for the first time, aiming to fluorinate the Li-stuffed garnet $Li_7La_3Zr_2O_{12}$ (LLZO) and create lithium vacancies (*i.e.*, to form the system $Li_{7-x}La_3Zr_2O_{12-x}F_x$), which our previous computational studies suggest should exhibit a change from tetragonal to cubic symmetry.[52] In addition, we investigate whether chlorination can be achieved using a similar synthetic route to produce $Li_{7-x}La_3Zr_2O_{12-x}Cl_x$. A comprehensive study, combining powder X-ray diffraction (XRD), solid-state nuclear magnetic resonance (NMR) spectroscopy, computational modelling and electrochemical testing is reported to investigate the effects of both F- and Cl-doping on the structure and the associated physical properties of halogenated LLZO. We also investigate the effects of surface fluorination on the performance of Al-doped LLZO ($Li_{6.4}Al_{0.2}La_3Zr_2O_{12}$, LLAZO).

Experimental

Synthesis of F(Cl)-doped $Li_7La_3Zr_2O_{12}$

Two routes were investigated for the halogenation of $Li_7La_3Zr_2O_{12}$. The first method utilised a standard high temperature synthesis route, in which stoichiometric amounts of lithium fluoride (99%, Alfa Aesar) or lithium chloride (99%, Sigma Aldrich), lithium carbonate (99%, Alfa Aesar), zirconium oxide (99%, Alfa Aesar) and lanthanide oxide (99.9%, Alfa Aesar) were mixed and ground using an agate mortar and pestle before being heated to 650 °C for 12 h. The mixture was subsequently ball milled for 30 min with 20% excess lithium carbonate, which was added to compensate for the loss of Li during the high temperature synthesis. The resulting powders were then pressed into pellets (13 mm diameter) using 0.2 tons pressure and heated to 1050 °C for 12 h.

For the second method, a sample of tetragonal $Li_7La_3Zr_2O_{12}$ was prepared *via* the route described above (omitting the addition of LiF or LiCl). The $Li_7La_3Zr_2O_{12}$ sample was then mixed with PTFE or PVC (polyvinyl chloride) powder in different molecular mass ratios (0.1PTFE equals $0.1CF_2CF_2$; 0.1PVC equals $0.1CH_2CHCl$). It is noted that, as a control, the reaction was also performed using the non-F(Cl)-containing polymer polyethylene (PE, 0.1PE equals $0.1CH_2CH_2$) to confirm the effect of F or Cl in the synthesis. Each mixture was transferred to an alumina boat and placed into a tube furnace for heat treatment under N_2. Dry N_2 gas was passed through the tube for 30 min before heating at 80 °C h^{-1} to 400–450 °C for 12 h with N_2 still flowing. The powders were reground and reheated at 80 °C h^{-1} to 400 °C for 12 h in air in a dry room with a dewpoint between −45 to −65 °C (Munters Ltd.) to try to remove any carbon byproduct. A dry room was used to prevent H/Li exchange, which is known to be an issue for garnet-based systems.

Surface fluorination of $Li_{6.4}Al_{0.2}La_3Zr_2O_{12}$

$Li_{6.4}Al_{0.2}La_3Zr_2O_{12}$ was prepared at 1000–1050 °C using the same method as for $Li_7La_3Zr_2O_{12}$ with the addition of Al_2O_3 (99%, Alfa Aesar). The $Li_{6.4}Al_{0.2}La_3Zr_2O_{12}$ powder was then pressed into a pellet (10 mm diameter) using 0.2 tons pressure, and heated at 1100 °C for 12 hours in a dry room, with parent powders on each side of the pellet. The pellet was polished using 400, 800, 1200, 2500, 4000 grinding papers, covered with PTFE powder on each side, and heated to 400 °C for 12 hours in the dry room to facilitate the surface fluorination process.

Characterisation of materials

Powder X-ray diffraction. Room and variable-temperature (VT) X-ray diffraction (XRD) data were collected using a Bruker

Open Access Article. Published on 04 May 2022. Downloaded on 12/12/2024 5:26:19 PM. This article is licensed under a Creative Commons Attribution 3.0 Unported Licence.

D8 X-ray diffractometer with a linear position sensitive detector (PSD) (CuK_α radiation 1.5418 Å). Room temperature XRD patterns were recorded over the 2θ range 10° to 60° with a 0.02° step size. VTXRD data of the heated precursor mixture were collected between 300 and 700 °C at 50 °C intervals. Structure refinement was carried out using the XRD data with the GSAS suite of Rietveld refinement software.[60]

Scanning electron microscopy (SEM). A HITACHI TM4000plus SEM with an energy dispersive X-ray spectroscopy (EDX) detector from AztecOne was used to probe both the microstructure and distribution of elements in the sample. Powders and pellets were applied to a carbon tape and analysed at 15 kV in backscattered electron mode.

Electrochemical testing of $Li_{6.4}Al_{0.2}La_3Zr_2O_{12}$. Li metal was hot pressed onto each side of the non-fluorinated/fluorinated $Li_{6.4}Al_{0.2}La_3Zr_2O_{12}$ pellets at 175 °C for 1 hour in an argon filled glove box. The Li/LLAZO/Li and Li/LLAZO(PTFE)/Li symmetric cells were then assembled using a Swagelok cell. These symmetric cells were cycled at various current densities to assess electrochemical stability at room temperature using a BioLogic VMP3 multichannel potentiostat. Electrochemical impedance spectroscopy (EIS) data was acquired using the impedance analyser attached to the BioLogic VMP3 multichannel potentiostat at 100 mV over the frequency range from 1 to 10^6 Hz.

Solid-state NMR spectroscopy. Solid-state ^{6,7}Li, ^{19}F and ^{35}Cl NMR spectra were acquired using a Bruker Avance III HD spectrometer equipped with a wide-bore 11.7 T magnet. Larmor frequencies of 73.6, 194.3, 470.6 and 49.0 MHz were used for ^{6}Li, ^{7}Li, ^{19}F and ^{35}Cl, respectively. Powdered samples were packed into conventional 4 mm ZrO_2 rotors inside a nitrogen-filled glovebag and a magic-angle spinning (MAS) rate of 10 kHz was employed. The ^{6,7}Li MAS NMR spectra were referenced to 1 M LiCl (aq), whilst the ^{19}F MAS NMR spectra were referenced to $CFCl_3$, carried out indirectly by setting the resonance from CF_3COOH/H_2O (50 : 50 v/v) to −76.54 ppm. The ^{35}Cl MAS NMR spectra were referenced to 0.1 M NaCl (aq).

Conventional ^{6}Li and ^{7}Li MAS NMR spectra were obtained using a single-pulse experiment with radiofrequency (rf) field strengths of 47.6–56 and 52.6–83 kHz, respectively. In order to suppress a large background signal, ^{19}F MAS NMR spectra were acquired using the "depth" pulse sequence. ^{35}Cl MAS NMR spectra were acquired using a Hahn-echo experiment utilising a rf field strength of 31.2 kHz. Specific experimental details are given in the corresponding figure captions.

Computational modelling. For the computational modelling the VASP code (version 5.4.4)[61] was employed which implements a planewave basis set with PAW pseudopotentials.[62] All calculations were spin polarised and used the PBEsol functional[63] with a 800 eV planewave cut-off energy. Energy minimisation employed a full geometry relaxation, including both atomic positions and lattice parameters. The electronic structure was optimized to an energy tolerance of 10^{-6} eV and the tolerance for ionic convergence was a force norm of 0.01 eV Å^{-1} for the geometry optimisations.

All LLZO systems were energy minimized in the tetragonal 192 atom unit cell (ICSD collection code 191528) using a converged 2 × 2 × 2 *k*-point grid. The simulation cells used for the bulk oxides comprised the anti-fluorite structure for Li_2O and the Baddeleyite structure for ZrO_2. Both the α-M_2O_3 and Bixbyite-M_2O_3 structures were calculated for lanthanum oxide and the lower energy polymorph used for further calculations (the more stable structure was found to be α-La_2O_3). The lithium halides all used the rocksalt structure. The Monkhorst–Pack *k*-point grid for all the pure oxide and halides materials was found to be converged at 4 × 4 × 4 grid points.

Defect calculations were first performed by inserting a single dopant halogen into the LLZO lattice without a compensating Li vacancy whose position is unknown or may be dynamic. Instead, the number of electrons was adjusted to maintain charge neutrality of the system. This setup is broadly equivalent to including an infinitely far away Li vacancy and allows comparison of halogen dopants on the different oxygen sites without the complication of a secondary local defect. Substitution on the cation sites has been ruled out by a previous study.[52] In the next stage Li vacancies are introduced as either a nearest neighbour or furthest neighbour to probe the tendency of the halogen and Li vacancy to cluster.

Results and discussion

Initial characterisation

A phase pure sample of tetragonal $Li_7La_3Zr_2O_{12}$ ($I4_1/acd$) was successfully prepared *via* conventional solid-state methods (Fig. 1), confirmed by Rietveld refinement using the PXRD data (Fig. S1†). However, attempts to produce F-doped samples, *e.g.*, $Li_{6.5}La_3Zr_2O_{11.5}F_{0.5}$, using similar high temperature methods led to a number of phases, including the desired tetragonal garnet phase, in addition to La_2O_3 and $La_2Zr_2O_7$ impurities, as shown in Fig. 1(a). Hence, there is no evidence of O replacement by F using LiF as a starting reagent *via* the standard high temperature synthesis route.

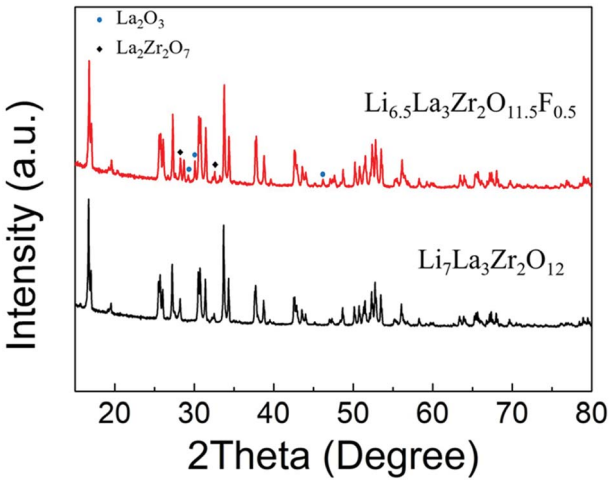

Fig. 1 XRD patterns obtained for $Li_{7-x}La_3Zr_2O_{12-x}F_x$: $x = 0$ and 0.5 showing significant impurities for $x = 0.5$ and no change in the level of tetragonal distortion; LiF was used as the fluorine source.

 This journal is © The Royal Society of Chemistry 2022

Open Access Article. Published on 04 May 2022. Downloaded on 12/12/2024 5:26:19 PM.
This article is licensed under a Creative Commons Attribution 3.0 Unported Licence.

In contrast, when the 'as prepared' tetragonal $Li_7La_3Zr_2O_{12}$ was mixed with PTFE and heated under dry N_2, a reduction in tetragonal distortion was observed as a function of PTFE content. Meanwhile, the parent $Li_7La_3Zr_2O_{12}$ sample (without addition of PTFE) showed no change upon heating under the same conditions (Fig. 2(a)). This suggests that the addition of PTFE was successful in causing a reduction in the tetragonal distortion, which is consistent with the incorporation of Li vacancies. This could be achieved either through the creation of O vacancies, $Li_{7-2x}La_3Zr_2O_{12-x}$, or *via* the incorporation of F^- in the place of O^{2-}, $Li_{7-x}La_3Zr_2O_{12-x}F_x$.

To determine if the observed phase transition is caused by the creation of oxide ion vacancies or F incorporation, a non-fluorine containing polymer, polyethylene (PE), was also investigated. The XRD patterns obtained for a sample prepared with PE are shown in Fig. 2(b), and the data clearly indicate unchanged tetragonal $Li_7La_3Zr_2O_{12}$ (Rietveld refinement of 1PE–LLZO is shown in Fig. S2†). This suggests that the changes observed are caused by the F in the PTFE polymer. Hence, this supports the hypothesis that F is incorporated into the garnet structure and its presence is required to deliver the observed reduction in tetragonal distortion.

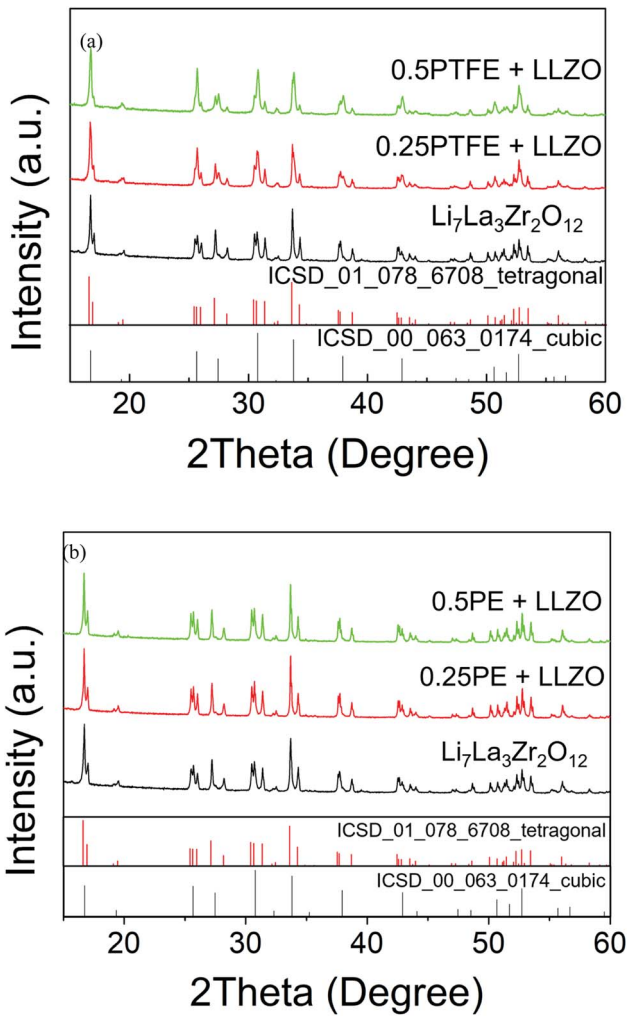

Fig. 2 XRD patterns obtained for samples of $Li_7La_3Zr_2O_{12}$ mixed with (a) PTFE and (b) PE at 400 °C in dry N_2, indicating a reduction in tetragonal distortion for the reaction with PTFE and no change upon reaction with PE.

0.2PTFE:LLZO was selected for further investigation, as the lithium content (~6.6) is usually considered optimal for Li conductivity in garnet systems. 0.2PTFE:LLZO was reground and reheated several times at 400–425 °C in both dry N_2 and air until no further change was detected by XRD. EDX mapping (Fig. 3(a)) indicated a homogeneous distribution of La, Zr, F and O throughout the 0.2PTFE:LLZO sample. The stability of the 0.2PTFE:LLZO sample was subsequently studied *via* variable-temperature XRD and is shown in Fig. 3(b). The XRD patterns obtained indicate that, above 500 °C, the cubic LLZOF phase undergoes partial decomposition. This begins with the formation of LaOF, followed by $LaZrF_7$ and ZrO_2 at higher temperature. This supports the inability to form the fluorinated phase *via* traditional high temperature solid state synthetic methods and corresponding studies of other mixed metal oxide fluorides (*e.g.*, perovskites and other related materials). This, therefore, suggests the F-containing garnet phase is metastable, thus requiring lower temperature routes for preparation.[56,64] This is also in agreement with the PXRD data collected for the sample synthesised using LiF as a starting reagent, where the fluorinated garnet phase could not be prepared *via* traditional high temperature solid state synthetic methods. Consequently, it was not possible to determine the conductivity of the fluorinated sample, as such an experiment would require high temperature sintering in order to obtain a dense pellet.

A similar issue was observed when LiCl was used as the Cl source for the synthesis of Cl-doped LLZO *via* traditional solid state synthetic methods (Fig. S3†). However, LLZOCl could successfully be synthesised *via* the polymer route. As shown in Fig. 4, a change from the tetragonal to cubic form was observed as the PVC content was increased. The observed and calculated patterns from refinement of 1PVC:LLZO are shown in Fig. S4,† and is in good agreement with the formation of the $Ia\bar{3}d$ cubic phase. The volume of 1PVC:LLZO increased from 2181.2 to 2206.7 Å^3, further supporting the successful incorporation of Cl in the LLZO structure, given the larger size of Cl^-, when compared to O^{2-}. Similar to the fluorinated samples, it was not possible to determine the conductivity as the high temperature instability means that pellet sintering is not possible without phase decomposition.

Computational modelling

In our previous work,[52] potential-based simulations suggested that fluoride anions are stable on the oxygen sites within LLZO with a compensating lithium-ion vacancy defect, which is consistent with the experimental results discussed above. Here, we further examine the position of the halide dopant and associated lithium vacancies in the LLZO framework. For each halide (F, Cl and Br), doping onto each of the three distinct O sites in LLZO were trialed. The energies were first calculated without the complicating presence of a lithium vacancy. The charge imbalance is compensated for instead by adjusting the

Open Access Article. Published on 04 May 2022. Downloaded on 12/12/2024 5:26:19 PM.
This article is licensed under a Creative Commons Attribution 3.0 Unported Licence.

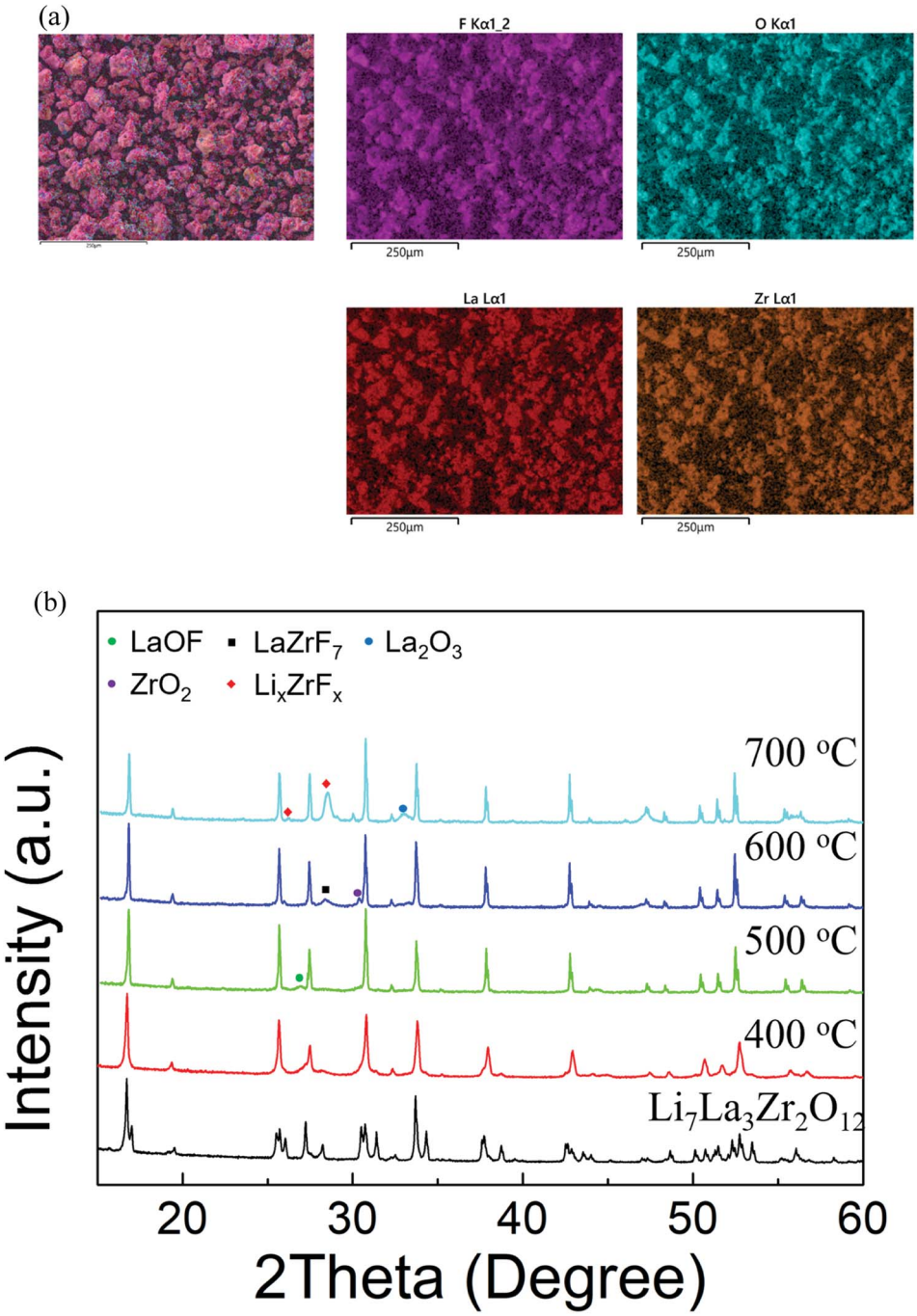

Fig. 3 (a) EDX elemental mapping images and (b) variable-temperature XRD patterns obtained for 0.2PTFE–LLZO. In (b) the formation of impurities is observed at $T > 500$ °C.

number of electrons in the system. This is equivalent to presuming the compensating lithium vacancy is infinitely far away and allows us to focus solely on the effect of the halide dopant.

Our DFT results show that for all three halogens the O2 site is preferred, followed by the O3 site and then the O1 site (Table 1). Interestingly the relative energies of doping F on different O sites have a comparatively small spread of 0.24 eV, compared to 0.48 eV for Cl and 0.67 eV for Br. In particular, the energy difference for doping F onto the O2 and O3 sites is very small (0.09 eV). This suggests that F is more likely to occupy multiple different O sites when doped into the LLZO structure than either Cl or Br, suggesting an increased disorder. The fully relaxed DFT structures of F-doped LLZO without Li vacancies are shown in Fig. 5.

Incorporating the lithium vacancy into the above calculations allows full defect calculations to be performed using the following mechanisms,

 This journal is © The Royal Society of Chemistry 2022

Open Access Article. Published on 04 May 2022. Downloaded on 12/12/2024 5:26:19 PM.
This article is licensed under a Creative Commons Attribution 3.0 Unported Licence.

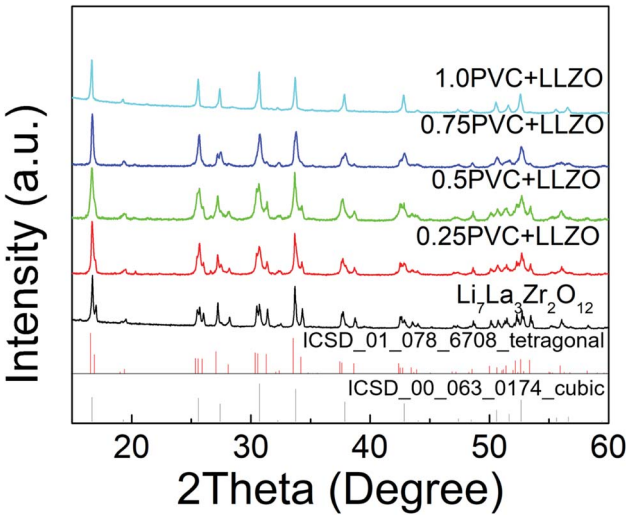

Fig. 4 XRD patterns obtained for samples of $Li_7La_3Zr_2O_{12}$ mixed with PVC showing formation of a cubic cell for higher Cl levels.

Table 1 Relative DFT energies of halogens on different O sites in LLZO, units of eV (note that comparisons cannot be made between different halides at this stage)

	F	Cl	Br
O1	0.24	0.48	0.67
O2	0.00	0.00	0.00
O3	0.09	0.38	0.56

$$\text{LLZO} + \text{LiF} \rightarrow \text{LLZO–F} + \text{Li}_2\text{O} \quad (1)$$

$$\text{LLZO} + \text{LiCl} \rightarrow \text{LLZO–Cl} + \text{Li}_2\text{O} \quad (2)$$

$$\text{LLZO} + \text{LiBr} \rightarrow \text{LLZO–Br} + \text{Li}_2\text{O} \quad (3)$$

Here, LiF, LiCl and LiBr are used to introduce the halides into the LLZO structure with the halogen on the oxygen site and a compensating Li vacancy. The compensating Li vacancies were introduced as either nearest or furthest neighbours to examine the tendency of the halogen and vacancy to cluster. The calculated defect energies are presented in Table 2.

Based on our findings, chlorine doping is ~0.6 eV less favorable than F doping, while Br doping is ~1.2 eV less favorable than F doping for any of the oxygen sites. Despite being less favourable, which can be attributed to the size of the halogen relative to the O site, the trends previously observed with only halogen doping still hold, with the O2 and O3 sites being the most favored sites for substitution. With F doping, the Li vacancy prefers to be located nearest to the F doped O site by 0.1–0.2 eV, irrespective of whether it is the O1, O2 or O3 site, suggesting a high degree of Li vacancy disorder which may favour transition of F-doped LLZO to the cubic phase (as observed in the PXRD data, *vide supra*). Fig. 6 shows the fully relaxed structure of LLZO with F doped on the most stable O3 site both with and without the nearest neighbour Li present.

For chlorine, the difference between the Li vacancy being a nearest and furthest neighbour from the dopant is more site dependent, with the O2 site showing the lowest difference in energies with the 'furthest neighbour' being ~0.3 eV higher in energy than 'nearest neighbour'. This difference increases to 0.8 eV for chlorine on the O3 site. For bromine, the Li vacancy binding to the dopant is even higher, with 0.5 eV for the O2 site and up to 1 eV for the O3 site, suggesting that both Cl and Br will trap Li vacancies even at higher temperatures. The preference to replace halogen with O2 sites (rather than O1 and O3) and/or the site dependence of lithium vacancies may be a further driving force for the experimentally observed decomposition of these phases at elevated temperatures.

Solid-state NMR studies

PTFE_LLZO. To gain further support for the incorporation of F and potential insight into the effects of F-doping on the LLZO garnet structure, ^{6,7}Li MAS NMR studies were completed for both the parent LLZO and the LLZOF sample prepared with a ratio of 0.25 PTFE:LLZO. The ^{7}Li MAS NMR spectra are shown in Fig. 7(a), where a single resonance centered at $\delta = 1.2$ ppm is exhibited in both, suggesting the presence of a single Li site. This is in contrast to the reported crystal structure ($Ia\bar{3}d$), where multiple lithium sites are observed.[13] The lack of resolved Li sites suggests that the local environments of the Li sites are very similar. This is quite typical of ^{6,7}Li NMR studies, owing to the very narrow chemical shift range. The presence of a single broad resonance could also suggest the presence of disorder within the system. Both isotopes of lithium can be studied using NMR spectroscopy. Typically, ^{7}Li is preferred due to its high natural abundance (92.5%). However, its larger quadrupole moment (-4.01 fm^2) can give rise to broad resonances, in particular for Li sites in low symmetry environments. Hence, ^{6}Li is often used to try and resolve overlapped resonances, as its lower quadrupole moment (-0.08 fm^2) results in narrower lineshapes.[65] The ^{6}Li MAS NMR spectra obtained for LLZOF and LZZO are shown in Fig. 7(b). Again, a single broad resonance is observed in both cases, further highlighting that the Li sites cannot be resolved. This is consistent with previous solid-state NMR studies of related Li-rich garnets, where sites have been shown to be overlapped, and so the data provide limited information about local structural changes caused by F incorporation.[66–68]

Consequently, the NMR studies were extended to include ^{19}F MAS NMR studies. DFT calculations (*vide supra*) suggest that the F anions are likely to disorder across the three O sites. In particular, doping onto O2 and O3 are only 0.09 eV different in energy. The ^{19}F MAS NMR spectrum of LLZOF is shown in Fig. 8(a). Here, a single resonance is observed at $\delta_{iso} = -123$ ppm with a manifold of spinning sidebands. As the sample was prepared using PTFE, it was important to determine the contribution of the PTFE to the ^{19}F MAS NMR spectrum relative to the F-doped LLZO. The ^{19}F MAS NMR spectrum of PTFE is shown in Fig. 8(b), where it is compared to the spectrum obtained for LLZOF. When compared, it is evident there is a considerable amount of PTFE still present within the sample. This suggests that the air heat treatment wasn't sufficient to

Open Access Article. Published on 04 May 2022. Downloaded on 12/12/2024 5:26:19 PM.
This article is licensed under a Creative Commons Attribution 3.0 Unported Licence.

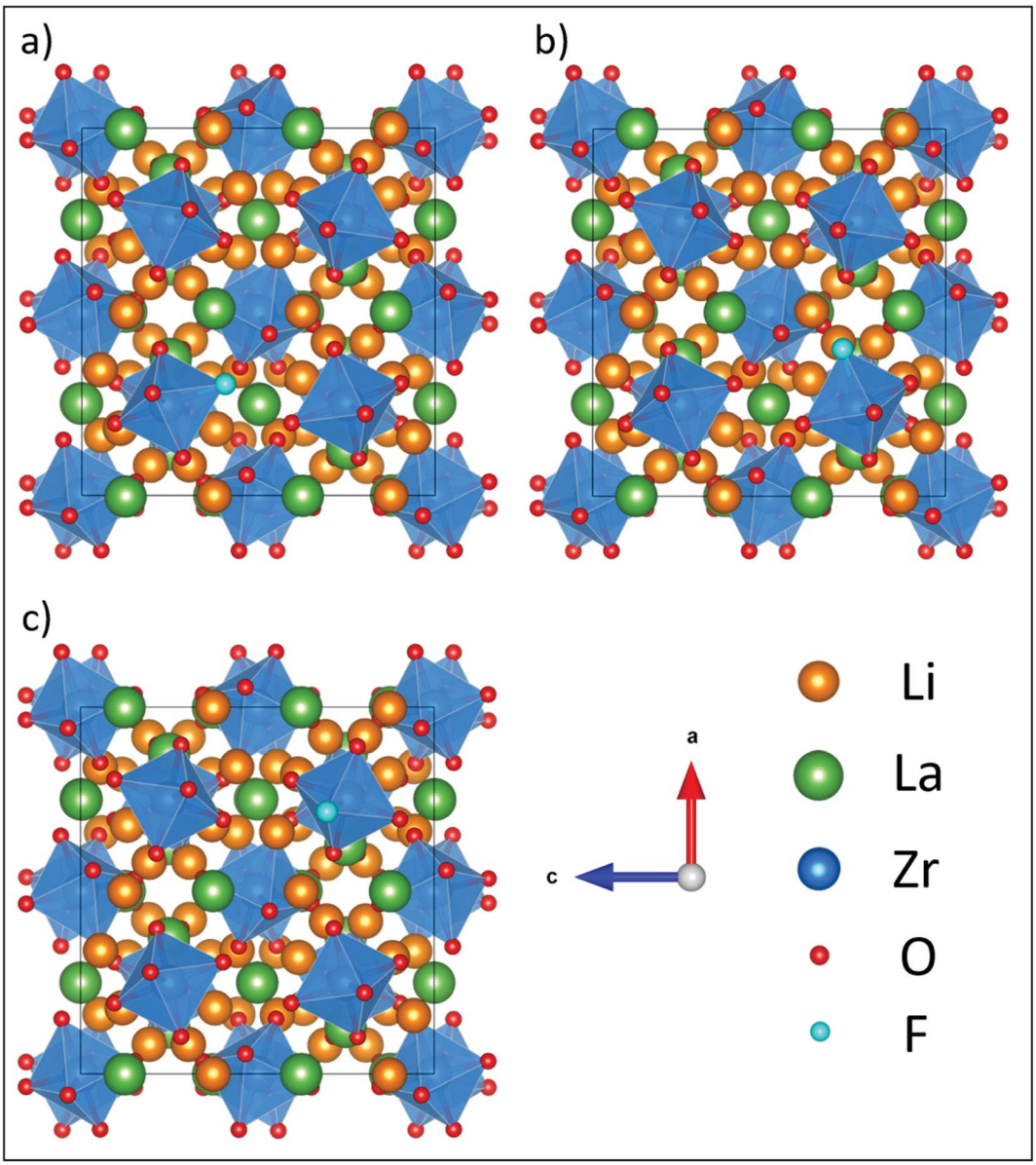

Fig. 5 Fully relaxed LLZO structures from DFT with an F defect on the (a) O1, (b) O2 and (c) O3 sites showing minimal disruption to the LLZO lattice. For simplicity, Li vacancies were not included in this set of calculations.

burn off any remaining PTFE, and so it indicates that either a higher temperature or longer times are needed. The PXRD data suggests that some of the F is successfully incorporated into the structure, reducing the tetragonal distortion (*vide supra*), and using solid-state ^{19}F MAS NMR spectroscopy it is possible to confirm the presence of F within the structure.

Table 2 Comparison of calculated defect energies for different halogen and Li vacancy defects arrangements in LLZO, units of eV

	Dopant					
	F		Cl		Br	
Li vacancy	Nearest neighbor	Furthest neighbor	Nearest neighbor	Furthest neighbor	Nearest neighbor	Furthest neighbor
O1	1.30	1.42	2.16	2.56	2.85	3.42
O2	1.11	1.22	1.78	2.07	2.25	2.72
O3	1.08	1.30	1.72	2.48	2.34	3.33

 This journal is © The Royal Society of Chemistry 2022

Open Access Article. Published on 04 May 2022. Downloaded on 12/12/2024 5:26:19 PM.
This article is licensed under a Creative Commons Attribution 3.0 Unported Licence.

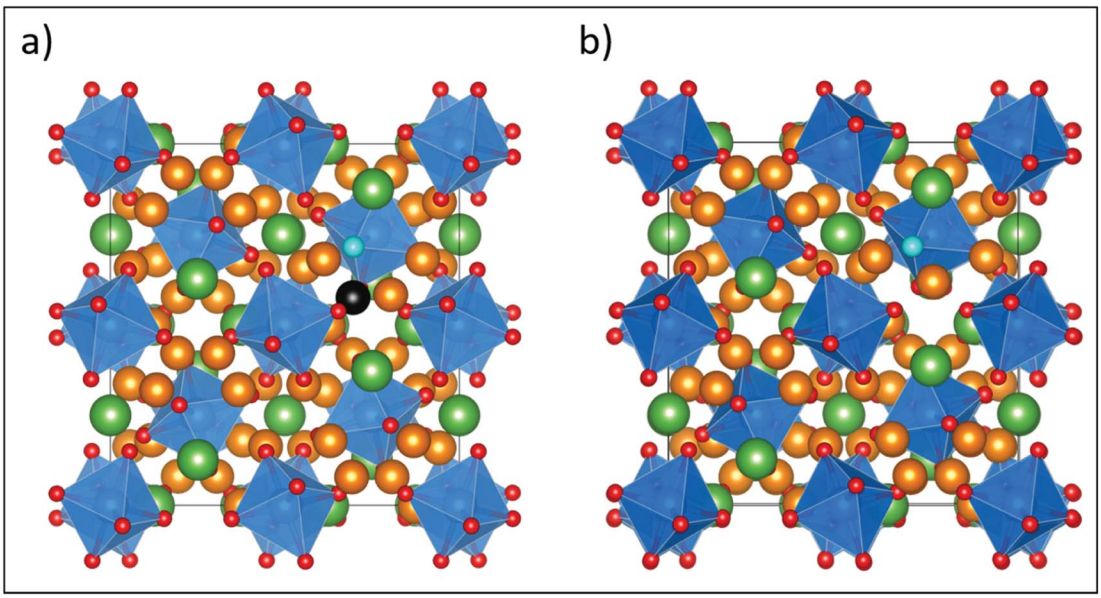

Fig. 6 Fully relaxed structures from DFT of the most stable F-doped LLZO configurations, where F is located on the O3 site with the nearest neighbour Li (highlighted in black) either (a) present or (b) removed, showing relaxation of a remaining Li away from its original lattice site towards the vacancy. The defect formation energy for this configuration is 1.08 eV (Table 2). Element colouring and cell orientation are the same as in Fig. 11.

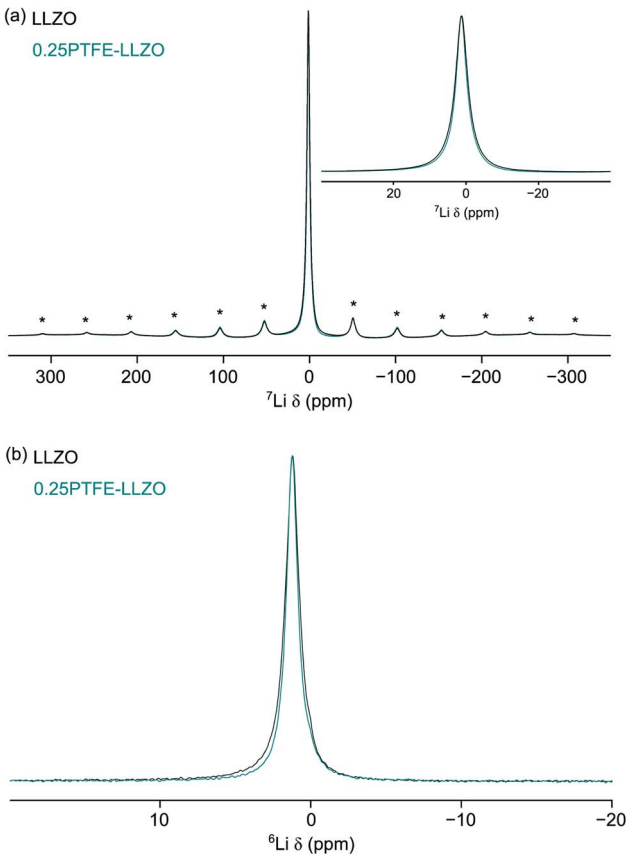

Fig. 7 (a) ^{7}Li and (b) ^{6}Li MAS NMR spectra obtained for LLZOF and LLZO. Spectra are the result of (a) 16, 32 and (b) 200 transients with a recycle interval of 90 s. A MAS rate of 10 kHz was used and spinning sidebands are denoted by *. In (a) an expansion of the central transition is also shown.

However, it is unfortunately not possible to accurately determine the precise location of the incorporated F, as the spectrum is dominated by the PTFE signal.

PVC_ LLZO. To gain an understanding of how Cl is substituted into the lithium-stuffed garnet structure, Cl-doped samples of LLZO (LLZOCl) were also analysed. ^{7}Li MAS NMR spectra were acquired for two samples with differing PVC contents, 0.75PVC:LLZO and 1.0PVC:LLZO, and are shown in Fig. 9(a) and (b), respectively. In both cases, two overlapping resonances are observed at $\delta \approx 1$ and 0 ppm. Based on our studies of LLZO, the broad resonance centred at $\delta \approx 1$ ppm is believed to correspond to the lithium environments in the LLZO structure. The sharper resonance, centred at $\delta \approx 0$ ppm, is only observed in the Cl-doped samples. As the PVC content is increased from 0.75PVC:LLZO to 1.0PVC:LLZO, the intensity of the sharp resonance increases relative to the broad resonance. To try and resolve the two resonances, ^{6}Li MAS NMR spectra were also acquired, and are shown in Fig. 10. Whilst the two resonances are not fully resolved using ^{6}Li MAS NMR, considerably better resolution is obtained. The broad peaks centred at $\delta = 1.31$ and 1.24 ppm for 0.75PVC:LLZO and 1.0PVC:LLZO, respectively, are shifted slightly compared to the lithium environment observed in the parent system LLZO ($\delta = 1.18$ ppm), which provides some direct support for the perturbation of the structure by the heat treatment with PVC, and hence support for the successful incorporation of Cl. The changes in chemical shift indicate subtle changes in the local structure, and thus the local environment of Li, as Cl is incorporated into the structure. Whilst we are unable to comment of the exact nature of the structural change, it is noted that the chemical shift for the 1.0PVC:LLZO is closer to that of LLZO than 0.75PVC:LLZO. The sharp peak, observed only in the LLZOCl samples, moves to

Open Access Article. Published on 04 May 2022. Downloaded on 12/12/2024 5:26:19 PM.
This article is licensed under a Creative Commons Attribution 3.0 Unported Licence.

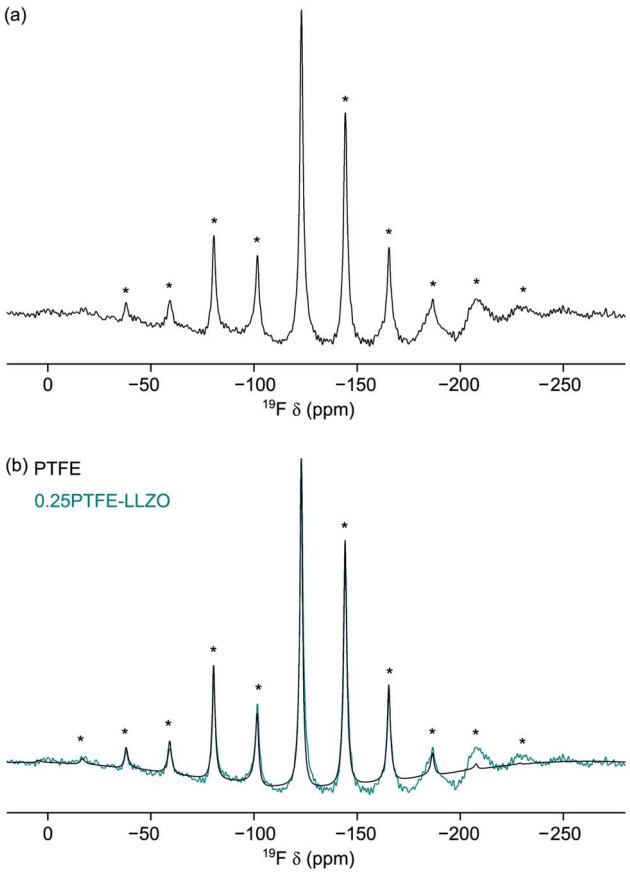

Fig. 8 ^{19}F MAS NMR spectra obtained for (a) LLZOF and (b) PTFE. In (b), the spectrum for LLZOF is also shown for comparison. Spectra are the result of (a) 320 and (b) 16 transients with a recycle interval of 10 s. A MAS rate of 10 kHz was used and spinning sidebands are denoted by *.

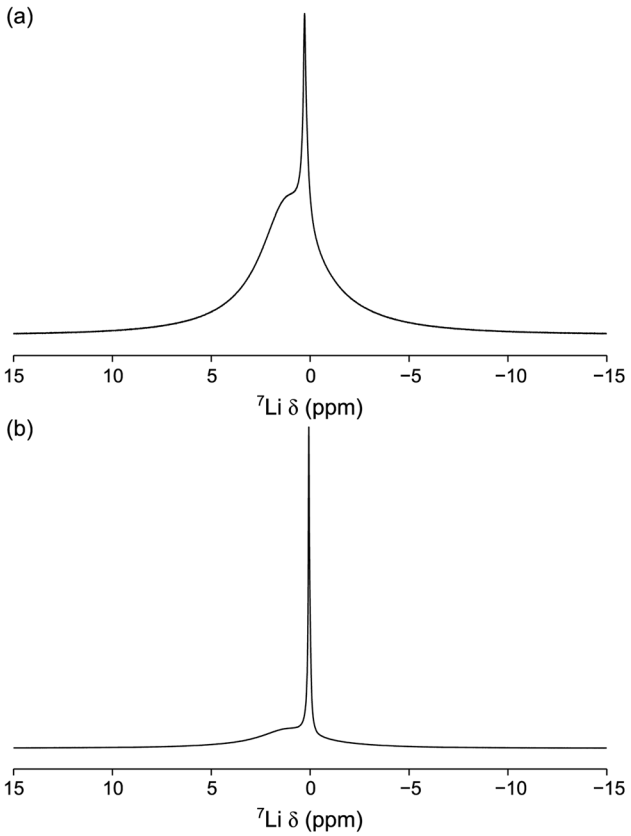

Fig. 9 ^{7}Li MAS NMR spectra of (a) 0.75PVC:LLZO and (b) 1.0PVC:LLZO. Each spectrum is the result of averaging 64 transients with a recycle interval of 6 s. A MAS rate of 10 kHz was used.

lower chemical shift as the PVC content increases, shifting from $\delta = 0.32$ ppm to $\delta = 0.09$ ppm. In both cases, this resonance is very sharp, suggesting it corresponds to lithium in a highly symmetrical environment. To try and assign these resonances, the chemical shifts were compared to those reported for a number of possible impurities, including LiCl(s) ($\delta = -1.1$ ppm). However, at present, it is unclear whether the presence of this additional lithium environment is a result of Cl-doping or an impurity introduced during synthesis.

The Cl environment within the Li-rich garnet structure can be studied directly using ^{35}Cl MAS NMR. The ^{35}Cl MAS NMR spectra obtained for 0.75PVC:LLZO and 1.0PVC:LLZO are shown in Fig. 11, where, in each case, a single resonance is observed. As the PVC content is increased, the resonance is shifted from $\delta = -0.27$ to 2.13 ppm and the peak narrows considerably. This indicates that, as more Cl is added to the system, the local Cl environment changes substantially, specifically, the Cl environment is becoming more symmetrical upon increased doping. It is currently unclear why increasing the PVC content effects the Cl local environment in such a dramatic way. Computational studies (*vide supra*) suggest that clustering of lithium vacancies near the dopant is favourable for Cl anions. This clustering has the potential to significantly influence the local structure of the doped system. However, further complementary studies, which are outside the remit of this study would be required to fully understand this local distortion. Overall, the NMR data provide evidence to support the successful incorporation of Cl, but further work is required to clarify the detailed structural features. For example, as previously suggested, total scattering studies would be useful in clarifying the changes to the local structure on halogen incorporation. Such studies would assist both the assignment and interpretation of the NMR data and DFT findings.

Effects of halogenation on electrochemical properties

As noted previously, it appears that the halogenation of $Li_7La_3Zr_2O_{12}$ is only successful at low temperatures, with heating to higher temperatures leading to partial phase decomposition. As a result, it was not possible to evaluate the effects of halogenation on the conductivity, as the thermal instability of halogenated $Li_7La_3Zr_2O_{12}$ meant that the samples could not be adequately sintered prior to conductivity measurements. Hence, instead, we investigated whether or not halogenation could be performed on a pre-sintered pellet of Al-doped LLZO ($Li_{6.4}Al_{0.2}La_3Zr_2O_{12}$) to form a surface layer which could potentially enhance the interfacial interaction with Li metal in an all-solid-state battery. As a result, these coatings could potentially be of interest for the reduction of interfacial resistance or prevention of dendrite growth.

 This journal is © The Royal Society of Chemistry 2022

Open Access Article. Published on 04 May 2022. Downloaded on 12/12/2024 5:26:19 PM.
This article is licensed under a Creative Commons Attribution 3.0 Unported Licence.

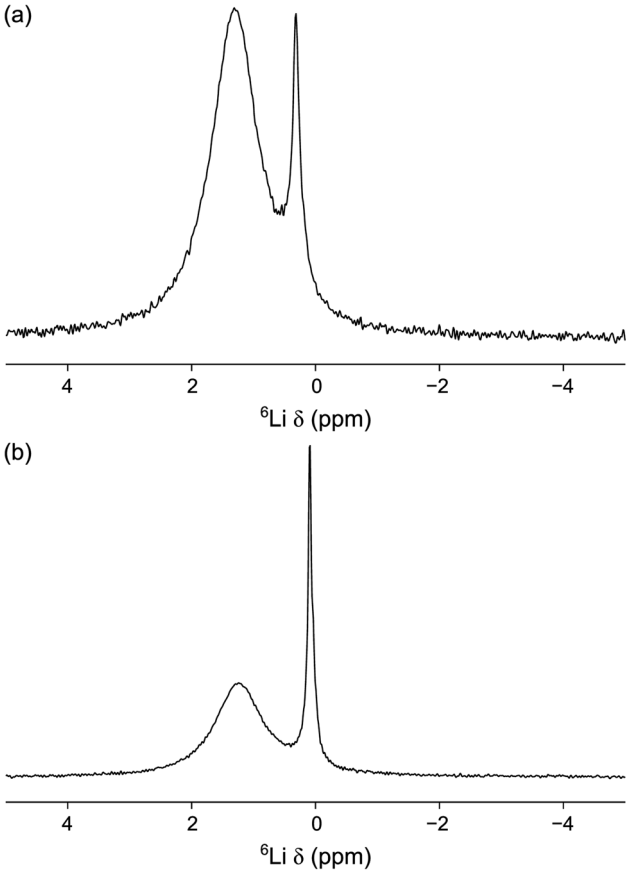

Fig. 10 ^{6}Li MAS NMR spectra of (a) 0.75PVC:LLZO and (b) 1.0PVC:LLZO. Each spectrum is the result of averaging 200 transients with a recycle interval of 8 s. A MAS rate of 10 kHz was used.

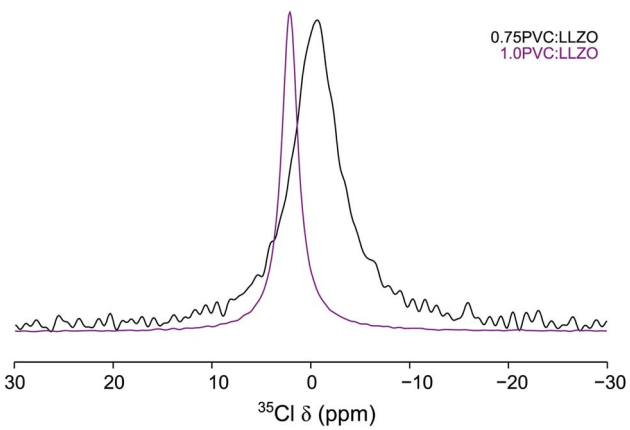

Fig. 11 ^{35}Cl MAS NMR spectra of 0.75PVC:LLZO and 1.0PVC:LLZO. Each spectrum is the result of averaging 1600 transients with a recycle interval of 0.4 s. A MAS rate of 10 kHz was used.

The Li/LLAZO/Li cell was initially tested, where short circuiting was observed at a low current density of around 0.1 mA cm^{-2} (Fig. S6 and S7†), which is a similar critical current density observed for LLAZO in the literature.[31] To evaluate the possible benefits of surface fluorination, the Li/LLAZO(PTFE)/Li symmetric cell was cycled with increasing current densities. The voltage of the cell slightly increased with increasing current densities (Fig. 12(a)). The voltage profile exhibits a slightly higher voltage on one side, which may be caused by uneven coating of the pellet. Two semicircles were observed in the EIS data (Fig. 12(b)). The first semicircle represents the total resistance of the garnet ceramic electrolyte (R_t), whilst the second (3171 Ω cm^2) is linked with the fluorinated coating and garnet/Li metal interface (R_i). During the cycling with increasing current densities, both R_t and R_i decreased (Fig. 12(c)). A particularly large decrease was observed for R_i, which decreased from 3171 to 751 Ω cm^2 at 0.1 mA cm^{-2} and 98 Ω cm^2 at 1 mA cm^{-2} (Fig. 12(c)). The cell was rested for 12 hours and the EIS data indicates a recovered total resistance of the garnet framework, indicating that the cell did not short circuit. It is noted that a slightly higher resistance is observed for the second semicircle after being rested (Fig. 12(b)), corresponding to the impedance of the F-doped layer.

In order to determine the critical current density of the cell, the current densities were increased from 1 mA cm^{-2} to 5 mA cm^{-2}. Similar results were observed, where the voltage of the cell remained ∼0.59 V at 1 mA cm^{-2} and increased with increasing current densities (Fig. 13(a)), and the resistance of the R_i decreased to ∼30 Ω cm^2 at 5 mA cm^{-2}. However, the EIS data obtained for the cell rested for 12 hours indicates only a small variation of the total resistance of the garnet after testing (Fig. 13(b)). Typically, an irreversible reduction of R would be expected due to dendrite penetration at higher currents. However, the data presented indicate the prevention of full dendrite penetration even with the applied high current density of 5 mA cm^{-2} (50 times higher than the value that gives a clear short circuit due to full Li dendrite penetration in the Li/LLAZO/Li cell) (Fig. 13(b)).

In order to evaluate the protective nature of these coatings further, higher current densities from 1 mA cm^{-2} to 10 mA cm^{-2} were then applied to the cell, and the voltage increased to 5.8 V at 10 mA cm^{-2} (Fig. 14(a)). In contrast to previous EIS data, R_i (515 Ω cm^2) increased at 10 mA cm^{-2} compared to those at 1 mA cm^{-2} (148 Ω cm^2, Fig. 14(c)). The R_i doubled as before, which may be attributed to some irreversible reaction(s) of the coating layer at higher voltages (XRD data after cycling testing is shown in Fig. S8†), whilst the R_t remains virtually the same after cycling at 10 mA cm^{-2}.

It is reported that local defects, such as void formation at the SSE/Li interface during the stripping process associated with reduction of SSE/Li contact area can result in increased polarisation and local current density, which triggers the dendrite formation and propagation in the solid state electrolyte.[69] In this work, EDX shows additional distribution of F over the LLAZO pellet after the PTFE treatment (shown in S9†), and we suggest that the surface fluorine incorporation (such as formation of fluorine containing phases, such as LiF[38]) may reduce the void formation in the LLAZO/Li interface, and consequently help to "smooth" the local current density and partially prevent the dendrite growth during the cycling. These preliminary results indicate that the fluorinated coating acts as a superior buffer layer that prevents full dendrite penetration at high current densities. It is noted that full optimisation of the fluorinated coating is currently ongoing and includes the

Open Access Article. Published on 04 May 2022. Downloaded on 12/12/2024 5:26:19 PM.
This article is licensed under a Creative Commons Attribution 3.0 Unported Licence.

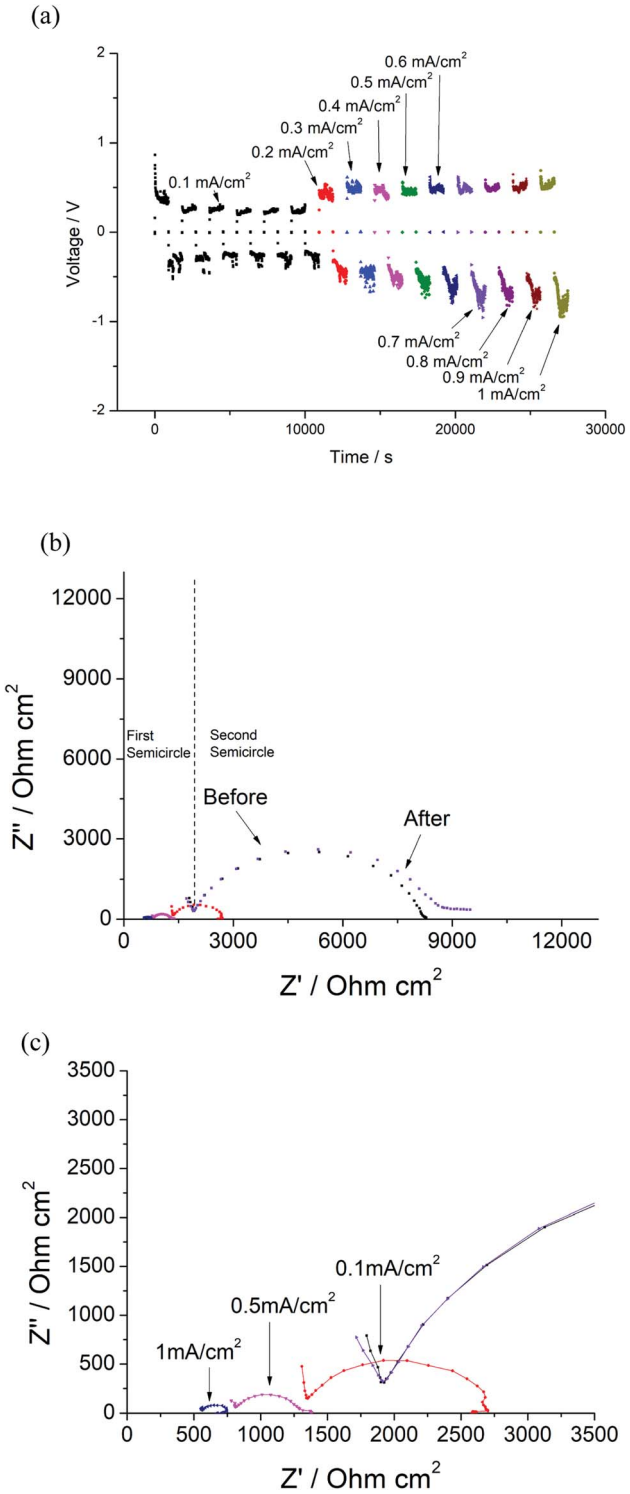

Fig. 12 (a) Constant current cycling testing of Li/LLAZO(PTFE)/Li cell from 0.1 mA cm^{-2} to 1 mA cm^{-2} (b) EIS of the cell before and after cycling. (c) EIS of the cell after 0.1 mA cm^{-2}, 0.5 mA cm^{-2} and 1 mA cm^{-2} cycling.

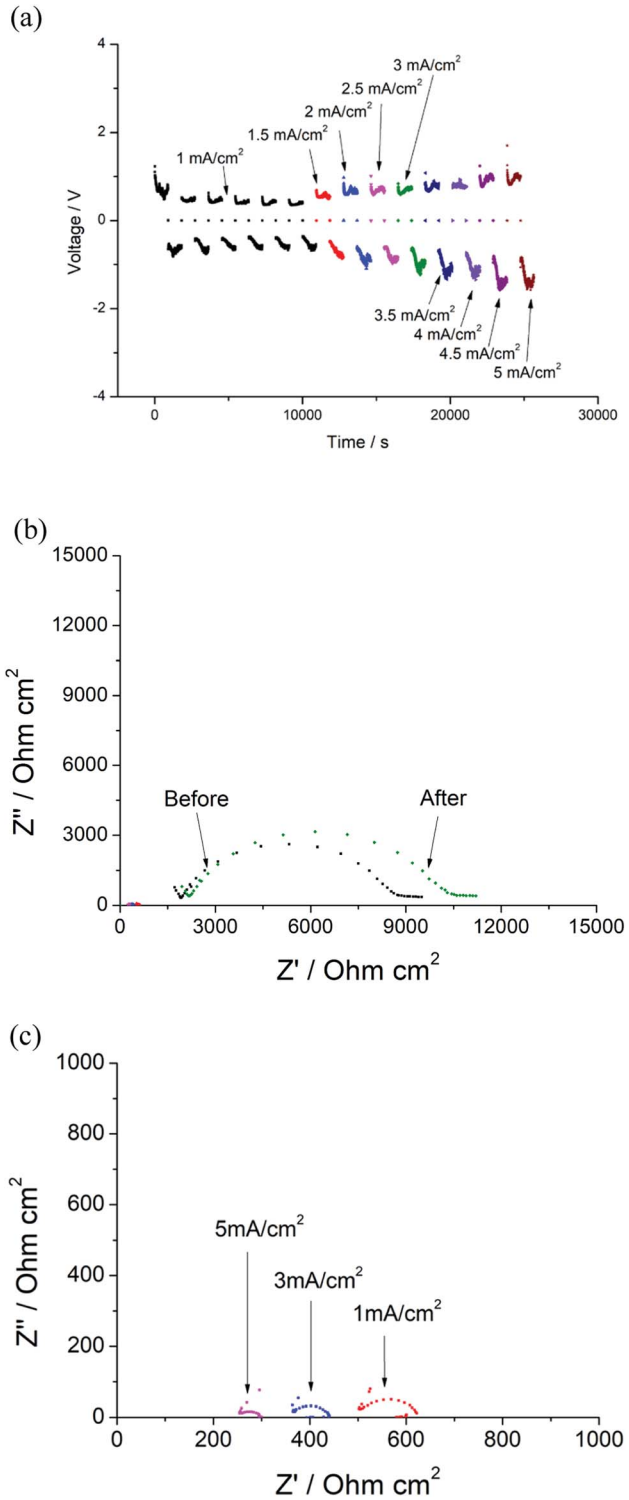

Fig. 13 (a) Constant current cycling testing of Li/LLAZO(PTFE)/Li cell from 1 mA cm^{-2} to 5 mA cm^{-2} (b) EIS of the cell before and after cycling. (c) EIS of the cell after 1 mA cm^{-2}, 3 mA cm^{-2} and 5 mA cm^{-2} cycling.

examination of thinner electrolyte membranes, the determination of the optimal layer thickness and temperature for fluorination and alternative F containing polymers, *e.g.*, PVDF, with a key future aim to attempt to reduce the interfacial resistance. Further surface characterisation, such as in-depth time-of-flight X-ray photoelectron spectroscopy (XPS), would be beneficial in gaining such information to support this hypothesis.

Open Access Article. Published on 04 May 2022. Downloaded on 12/12/2024 5:26:19 PM.
This article is licensed under a Creative Commons Attribution 3.0 Unported Licence.

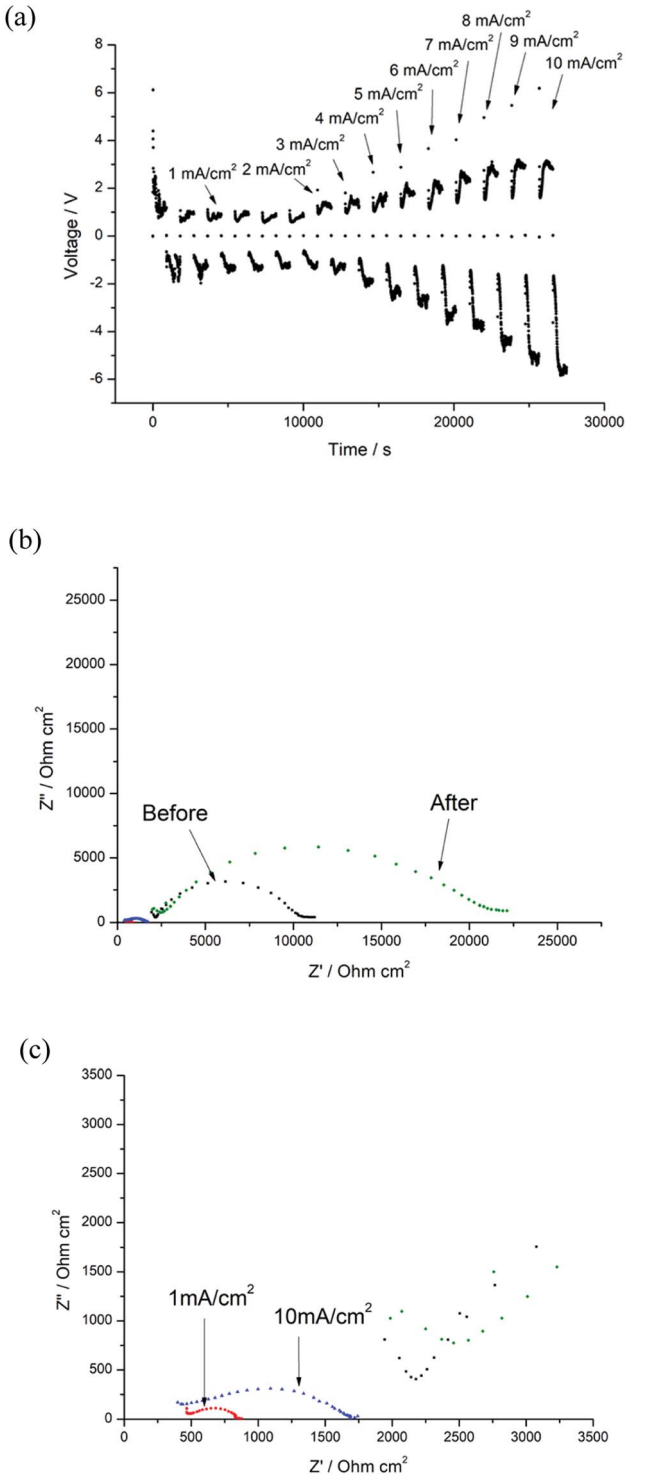

Fig. 14 (a) Constant current cycling testing of Li/LLAZO(PTFE)/Li cell from 1 mA cm^{-2} to 10 mA cm^{-2} (b) EIS of the cell before and after cycling. (c) EIS of the cell after 1 mA cm^{-2} and 10 mA cm^{-2} cycling.

Conclusions

The present study is the first example of a low temperature polymer halogenation (F, Cl) of the solid electrolyte material $Li_7La_3Zr_2O_{12}$. Upon halogenation, a reduction in tetragonal distortion is observed for F doping while a phase transformation from tetragonal to cubic symmetry is observed for Cl doping, which agrees with the creation of lithium vacancies, owing to the replacement of O^{2-} with F^- or Cl^-. Our computational studies suggest F-doping is more energetically favourable than Cl- and Br-doping (the latter not studied experimentally) and indicate that the O2 and O3 sites are the most favourable for substitution. Using solid-state NMR spectroscopy, the presence of F in F-doped LLZO was confirmed, in addition to residual PTFE from the synthesis process. Unfortunately, it was not possible to locate the precise position of each species within the structure using ^{6,7}Li and ^{19}F MAS NMR spectroscopy. ^{7}Li and ^{6}Li MAS NMR suggest two Li environments, one corresponding to lithium in a highly symmetrical environment. The ^{35}Cl MAS NMR spectra exhibit narrowing of the lineshape, suggesting the Cl environment becomes more symmetrical upon increased doping. Despite successful halogenation of LLZO, the instability at high temperatures means that such anion doped garnets cannot be successfully sintered to evaluate the effect on the conductivity. Nevertheless, we have demonstrated the same approach can be used to produce a fluorinated coating layer on sintered Al-doped LLZO. Electrochemical evaluation indicates that this fluorinated coating layer acts as a superior buffer that prevents full dendrite penetration at high current densities, up to 10 mA cm^{-2}.

Conflicts of interest

There are no conflicts of interest to declare.

Acknowledgements

PRS and BD acknowledge the support of the EPSRC grant EP/R024006/1: ICSF Wave 1: GENESIS: Garnet Electrolytes for New Energy Storage Integrated Solutions, and EPSRC grant EP/T02349X/1 Capitol Award for Core Equipment. We would like to thank the University of Birmingham for the studentship funding of MPS and MSJ. KEJ and ARH would like to thank Dr David Apperley for experimental assistance and the EPRSC for an EPSRC Doctoral Partnership award (EP/N509462/1). PG and SRY acknowledge the support of EPSRC SUPERGEN grant, EP/N001982/1. PG and SRY are grateful for the use of the 'Hydra' High Performance System at Loughborough University in addition to time on the ARCHER UK National Supercomputing Service (http://www.archer.ac.uk) supplied *via* our membership of the UK's HEC Materials Chemistry Consortium, which is funded by EPSRC (EP/L000202, EP/R029431). PG and SRY strongly acknowledge the use of Athena as part of the HPC Midlands+ consortium, funded by the EPSRC on grant EP/P020232/1. Raw experimental data can be found at: https://doi.org/10.25500/edata.bham.00000799.

References

1 J.-M. Tarascon and M. Armand, *Nature*, 2001, **414**, 359–367.
2 P. G. Bruce, B. Scrosati and J. M. Tarascon, *Angew. Chem., Int. Ed.*, 2008, **47**, 2930–2946.

Open Access Article. Published on 04 May 2022. Downloaded on 12/12/2024 5:26:19 PM.
This article is licensed under a Creative Commons Attribution 3.0 Unported Licence.

3 J. B. Goodenough and K. S. Park, *J. Am. Chem. Soc.*, 2013, **135**, 1167–1176.
4 Y. Wang, W. D. Richards, S. P. Ong, L. J. Miara, J. C. Kim, Y. Mo and G. Ceder, *Nat. Mater.*, 2015, **14**, 1026–1031.
5 V. Thangadurai, S. Narayanan and D. Pinzaru, *Chem. Soc. Rev.*, 2014, **43**, 4714–4727.
6 B. Dong, R. Jarkaneh, S. Hull, N. Reeves-McLaren, J. J. Biendicho and A. R. West, *J. Mater. Chem. A*, 2016, **4**, 1408–1413.
7 S. Ramakumar, C. Deviannapoorani, L. Dhivya, L. S. Shankar and R. Murugan, *Prog. Mater. Sci.*, 2017, **88**, 325–411.
8 N. Zhao, W. Khokhar, Z. Bi, C. Shi, X. Guo, L.-Z. Fan and C.-W. Nan, *Joule*, 2019, **3**, 1190–1199.
9 A. J. Samson, K. Hofstetter, S. Bag and V. Thangadurai, *Energy Environ. Sci.*, 2019, **12**, 2957–2975.
10 B. Dong, M. P. Stockham, P. A. Chater and P. R. Slater, *Dalton Trans.*, 2020, **49**, 11727–11735.
11 V. Thangadurai, H. Kaack and W. Weppner, *J. Am. Ceram. Soc.*, 2003, **86**, 437–440.
12 R. Murugan, V. Thangadurai and W. Weppner, *Angew. Chem., Int. Ed.*, 2007, **46**, 7778–7781.
13 J. Awaka, N. Kijima, H. Hayakawa and J. Akimoto, *J. Solid State Chem.*, 2009, **182**, 2046–2052.
14 G. Larraz, A. Orera and M. L. Sanjuán, *J. Mater. Chem. A*, 2013, **1**, 11419–11428.
15 V. Thangadurai and W. Weppner, *Adv. Funct. Mater.*, 2005, **15**, 107–112.
16 M. A. Howard, O. Clemens, E. Kendrick, K. S. Knight, D. C. Apperley, P. A. Anderson and P. R. Slater, *Dalton Trans.*, 2012, **41**, 12048–12053.
17 M. A. Howard, O. Clemens, K. S. Knight, P. A. Anderson, S. Hafiz, P. M. Panchmatia and P. R. Slater, *J. Mater. Chem. A*, 2013, **1**, 14013–14022.
18 H. El Shinawi and J. Janek, *J. Power Sources*, 2013, **225**, 13–19.
19 A. G. Squires, D. O. Scanlon and B. J. Morgan, *Chem. Mater.*, 2019, **32**, 1876–1886.
20 B. Dong, L. L. Driscoll, M. P. Stockham, E. Kendrick and P. R. Slater, *Solid State Ionics*, 2020, **350**, 115317.
21 M. P. Stockham, A. A. Griffiths, B. Dong and P. R. Slater, *Chem.–Eur. J.*, 2021, **27**, 1–10.
22 C. Galven, J.-L. Fourquet, M.-P. Crosnier-Lopez and F. o. Le Berre, *Chem. Mater.*, 2011, **23**, 1892–1900.
23 L. Truong, M. Howard, O. Clemens, K. S. Knight, P. R. Slater and V. Thangadurai, *J. Mater. Chem. A*, 2013, **1**, 13469–13475.
24 R. H. Brugge, A. K. O. Hekselman, A. Cavallaro, F. M. Pesci, R. J. Chater, J. A. Kilner and A. Aguadero, *Chem. Mater.*, 2018, **30**, 3704–3713.
25 H. Huo, J. Luo, V. Thangadurai, X. Guo, C.-W. Nan and X. Sun, *ACS Energy Lett.*, 2019, **5**, 252–262.
26 C. Wang, K. Fu, S. P. Kammampata, D. W. McOwen, A. J. Samson, L. Zhang, G. T. Hitz, A. M. Nolan, E. D. Wachsman, Y. Mo, V. Thangadurai and L. Hu, *Chem. Rev.*, 2020, **120**, 4257–4300.
27 S. Ohta, M. Kawakami, H. Nozaki, C. Yada, T. Saito and H. Iba, *J. Mater. Chem. A*, 2020, **8**, 8989–8996.
28 E. J. Cussen, *J. Mater. Chem.*, 2010, **20**, 5167–5173.
29 M. P. Stockham, B. Dong, M. S. James, Y. Li, Y. Ding, E. Kendrick and P. R. Slater, *Dalton Trans.*, 2021, **50**, 13786–13800.
30 K. Park, B.-C. Yu, J.-W. Jung, Y. Li, W. Zhou, H. Gao, S. Son and J. B. Goodenough, *Chem. Mater.*, 2016, **28**, 8051–8059.
31 F. M. Pesci, R. H. Brugge, A. K. O. Hekselman, A. Cavallaro, R. J. Chater and A. Aguadero, *J. Mater. Chem. A*, 2018, **6**, 19817–19827.
32 P. Canepa, J. A. Dawson, G. Sai Gautam, J. M. Statham, S. C. Parker and M. S. Islam, *Chem. Mater.*, 2018, **30**, 3019–3027.
33 R. H. Brugge, F. M. Pesci, A. Cavallaro, C. Sole, M. A. Isaacs, G. Kerherve, R. S. Weatherup and A. Aguadero, *J. Mater. Chem. A*, 2020, **8**, 14265–14276.
34 B. Tang, L. Gao, J. Liu, S.-H. Bo, Z. Xie, J. Wei and Z. Zhou, *J. Mater. Chem. A*, 2020, **8**, 18087–18093.
35 K. J. Kim and J. L. M. Rupp, *Energy Environ. Sci.*, 2020, **13**, 4930–4945.
36 F. Flatscher, M. Philipp, S. Ganschow, H. M. R. Wilkening and D. Rettenwander, *J. Mater. Chem. A*, 2020, **8**, 15782–15788.
37 L. Yang, Z. Lu, Y. Qin, C. Wu, C. Fu, Y. Gao, J. Liu, L. Jiang, Z. Du, Z. Xie, Z. Li, F. Kong and G. Yin, *J. Mater. Chem. A*, 2021, **9**, 5952–5979.
38 S. Tang, G. Chen, F. Ren, H. Wang, W. Yang, C. Zheng, Z. Gong and Y. Yang, *J. Mater. Chem. A*, 2021, **9**, 3576–3583.
39 X. Han, Y. Gong, K. K. Fu, X. He, G. T. Hitz, J. Dai, A. Pearse, B. Liu, H. Wang, G. Rubloff, Y. Mo, V. Thangadurai, E. D. Wachsman and L. Hu, *Nat. Mater.*, 2017, **16**, 572–579.
40 Y. Li, X. Chen, A. Dolocan, Z. Cui, S. Xin, L. Xue, H. Xu, K. Park and J. B. Goodenough, *J. Am. Chem. Soc.*, 2018, **140**, 6448–6455.
41 J. Dai, C. Yang, C. Wang, G. Pastel and L. Hu, *Adv. Mater.*, 2018, **30**, 1802068.
42 W. Zhou, Z. Wang, Y. Pu, Y. Li, S. Xin, X. Li, J. Chen and J. B. Goodenough, *Adv. Mater.*, 2019, **31**, 1805574.
43 Y. Ruan, Y. Lu, X. Huang, J. Su, C. Sun, J. Jin and Z. Wen, *J. Mater. Chem. A*, 2019, **7**, 14565–14574.
44 B. Dong, S. R. Yeandel, P. Goddard and P. R. Slater, *Chem. Mater.*, 2019, **32**, 215–223.
45 S.-S. Chi, Y. Liu, N. Zhao, X. Guo, C.-W. Nan and L.-Z. Fan, *Energy Storage Mater.*, 2019, **17**, 309–316.
46 J. Fu, P. Yu, N. Zhang, G. Ren, S. Zheng, W. Huang, X. Long, H. Li and X. Liu, *Energy Environ. Sci.*, 2019, **12**, 1404–1412.
47 H. Huo, Y. Chen, R. Li, N. Zhao, J. Luo, J. G. Pereira da Silva, R. Mücke, P. Kaghazchi, X. Guo and X. Sun, *Energy Environ. Sci.*, 2020, **13**, 127–134.
48 M. P. Stockham, B. Dong, M. S. James, Y. Li, Y. Ding and P. R. Slater, *Dalton Trans.*, 2021, **50**, 2364–2374.
49 A. I. Waidha, T. Ferber, M. Donzelli, N. Hosseinpourkahvaz, V. Vanita, K. Dirnberger, S. Ludwigs, R. Hausbrand, W. Jaegermann and O. Clemens, *ACS Appl. Mater. Interfaces*, 2021, **13**, 31111–31128.
50 W. Ping, C. Wang, Z. Lin, E. Hitz, C. Yang, H. Wang and L. Hu, *Adv. Energy Mater.*, 2020, **10**, 2000702.
51 A. Parejiya, R. Amin, R. Essehli, D. L. Wood and I. Belharouak, *ACS Energy Lett.*, 2020, **5**, 3368–3373.

 This journal is © The Royal Society of Chemistry 2022

Open Access Article. Published on 04 May 2022. Downloaded on 12/12/2024 5:26:19 PM.
This article is licensed under a Creative Commons Attribution 3.0 Unported Licence.

52 S. R. Yeandel, B. J. Chapman, P. R. Slater and P. Goddard, *J. Phys. Chem. C*, 2018, **122**, 27811–27819.
53 Y. Lu, X. Meng, J. A. Alonso, M. T. Fernandez-Diaz and C. Sun, *ACS Appl. Mater. Interfaces*, 2019, **11**, 2042–2049.
54 C. Liu, Z. Y. Wen and K. Rui, *J. Inorg. Mater.*, 2015, **30**, 995–1001.
55 B. Dong, J. Yan, B. Walkley, K. K. Inglis, F. Blanc, S. Hull and A. R. West, *Solid State Ionics*, 2018, **327**, 64–70.
56 P. R. Slater and R. K. B. Gover, *J. Mater. Chem.*, 2002, **12**, 291–294.
57 P. R. Slater, *J. Fluorine Chem.*, 2002, **117**, 43–45.
58 O. Clemens and P. R. Slater, *Rev. Inorg. Chem.*, 2013, **33**, 105–117.
59 M. A. Nowroozi, K. Wissel, J. Rohrer, A. R. Munnangi and O. Clemens, *Chem. Mater.*, 2017, **29**, 3441–3453.
60 B. H. Toby, *J. Appl. Crystallogr.*, 2001, **34**, 210–213.
61 G. Kresse and J. Hafner, *Phys. Rev. B: Condens. Matter Mater. Phys.*, 1994, **49**, 14251–14269.
62 P. E. Blochl, *Phys. Rev. B: Condens. Matter Mater. Phys.*, 1994, **50**, 17953–17979.
63 J. P. Perdew, A. Ruzsinszky, G. I. Csonka, O. A. Vydrov, G. E. Scuseria, L. A. Constantin, X. Zhou and K. Burke, *Phys. Rev. Lett.*, 2008, **100**, 136406.
64 O. Clemens, R. Haberkorn, P. R. Slater and H. P. Beck, *Solid State Sci.*, 2010, **12**, 1455–1463.
65 K. J. D. Mackenzie and M. E. Smith, *Multinuclear Solid-State NMR of Inorganic Materials*, Pergamon: Oxford, 2002.
66 S. Narayanan, V. Epp, M. Wilkening and V. Thangadurai, *RSC Adv.*, 2012, **2**, 2553–2561.
67 P. Bottke, D. Rettenwander, W. Schmidt, G. Amthauer and M. Wilkening, *Chem. Mater.*, 2015, **27**, 6571–6582.
68 J. Percival, D. Apperley and P. R. Slater, *Solid State Ionics*, 2008, **179**, 1693–1696.
69 J. Kasemchainan, S. Zekoll, D. Spencer Jolly, Z. Ning, G. O. Hartley, J. Marrow and P. G. Bruce, *Nat. Mater.*, 2019, **18**, 1105–1111.